IAC—22.D3.2B.x68580

THE "SENSIBLE" WAY TO CONSTRUCT ROBOTS FROM LUNAR RESOURCES

Alex Ellery
Carleton University, Canada, aellery@mae.carleton.ca

We explore how one specific aspect of robotic machines – sensors – may be constructed from lunar resources. Sensors constitute one member of the sensors-controller-actuators backbone of robotics. We focus on two families of sensor – displacement sensors and their derivatives as the most fundamental of measurements and light sensor arrays for general measurement-at-a-distance. Terrestrial approaches may not be appropriate to accommodate the constraints imposed by the Moon and our projected manufacturing capabilities. Potentiometers of aluminium extracted from anorthite offer access to displacement sensing and strain sensing. Piezoelectric sensors may be constructed from quartz manufactured from silica extracted from anorthite. Elastomeric silicone plastic derived from lunar volatile condensates offer the potential for tactility. Light sensors may be constructed from photomultiplier tubes, all components of which can be derived from lunar material. Photomultiplier tube resolution is limited but small rather than large arrays may be employed. We can exploit biomimetic approaches - optic flow offers the visual capabilities of insects using simple circuitry; active vision allows us to trade the deficiencies of the visual resolution with that of orienting motors through micro-stepping. We also explore the possibility of simple analytical instrumentation constructed from lunar resources. We suggest that rudimentary sensors can be constructed in-situ from lunar resources as fundamental components of robotic machines essential for a sustainable extraterrestrial infrastructure.

I. INTRODUCTION

Most interest to date regarding in-situ resource utilisation (ISRU) has been in sourcing bulk material for structure building and consumables (especially propellant) because of its high cost of transport from Earth. Such bulk products tend to be of low complexity and so functionally reliable over long periods. An implicit assumption has always been that highly sophisticated items will be transported from Earth – however, this precludes the prospect of repair or replacement on site. More complex items such as electronics and motors tend to suffer from greater failure rates. It would be advantageous to pursue the potential exploitation of local in-situ resources for more sophisticated products than passive structure (such as regolith and/or metals like aluminium) and volatile consumables (such as water). Although in-situ bulk materials reduce the cost of lunar exploration dramatically, true sustainability requires lunar self-sufficiency through enhanced in-situ resource utilisation. Self-sufficiency requires in-situ manufacture of the machines of production, i.e. robotic machines. Indeed, sustainability of a Moon Village and any associated infrastructure will require the ability to maintain and grow itself. We submit that such enhanced capability should encompass the construction of the robotic machines that build infrastructure. In this way, the robotic machines of production required to construct lunar infrastructure, as well as the infrastructure itself, may be leveraged from the lunar environment. The characteristic backbone of robotic machines is the sensorimotor control system – sensors, motors and computational electronics. We focus on in-situ manufacture of sensors from lunar resources here. Indeed, sensors and actuators are intimately related. For example, brushless electronic commutation requires stator windings to have Hall effect (or other displacement) sensors mounted to detect the position of the rotor for closed loop control. This effectively provides for the implementation of position and velocity feedback in a servomotor. A particularly explicit example of sensor-actuator coupling is apparent in active vision that is addressed later.

Measurement of physical properties begins with dimensional analysis of sensory transduction mechanisms. In dimensional analysis, the fundamental dimensions are amount [N], mass [M], length [L], time [T], temperature [Θ], electric current [I] and luminosity [J]. All sensory measurements are derived from these fundamental physical properties. We focus on two families of sensor – displacement sensors and their derivatives as the most fundamental measurements and light sensors for general measurement-at-a-distance. These sensory modalities relate directly to the determination of internal state (displacement-acceleration-force-pressure) and external state (vision). These are crucial to the implementation of motor control systems for robotic devices and/or smart lunar bases – imaging cameras and displacement/tactile sensing. These are also fundamental to 3D printing machines of production necessary to build lunar bases through contour crafting [1] or D-shaping [2]. We explore initially the use of electrical resistance and piezoelectric quartz for the measurement of fundamental mechanical

parameters. We then explore the prospect of sourcing photomultiplier tube (PMT) construction on the Moon as a flagship indicator that sophisticated sensors can be built using lunar resources. Our arguments stem directly from our lunar industrial ecology concept [3] (Appendix). We address some of the limits of lunar resources and how we might exploit bio-inspired approaches to compensate for these limitations.

II. DISPLACEMENT & DERIVED PARAMETER SENSING

Displacement is the most fundamental of measurements from which many others are derived. The simplest form of displacement sensor is the potentiometer, a tapped resistance wire in a voltage divider configuration. Of course, resistive components may be constructed from aluminium metal extracted from lunar anorthite (e.g. [4]). Derived from this is the measurement of temperature, strain, stress, pressure, acceleration and force. Humidity, temperature and strain sensors have been 3D printed (using inkjet and screenprinting) primarily based on conductive metals such as Ag, conductive polymers such as PEDOT:PSS (poly(3,4-ethylenedioxyrgophene) polystyrene sulphonate) or piezoelectrics such as PVDF (poly(vinylidenefluoride)) on flexible or rigid substrates [5]. A strain gauge comprises a meandered conductive strip of metal (such as aluminium or nickel) which when deformed through stress exhibits a change in resistance measured with a Wheatstone bridge. The campaniform sensillum in insects shows a similar approach to strain gauge design – it comprises an elliptical hole in a plate of cuticle in which chitin fibres surround the hole acting as strain gauges [6].

Pressure is defined as force/unit area which forms the basis of tactile sensing (taction). Tactile sensors detect physical contact with the environment and are based on deformation. In mammalian biology, feedback from muscles is generated by the spindles (position-derivative) and Golgi tendon sensors (force) which provides local muscular force feedback. Tactile sensing is a complex sensory modality that is mediated in human skin by four mechanoreceptors with a spatial resolution of 1 mm^2: (i) Pacinian corpuscles deep within the dermis exhibit fast adaptation to touch and vibration, (ii) Meissner corpuscles immediately beneath the epidermis exhibit moderate adaptation to touch and touch rate, (iii) Merkel discs exhibit slow adaptation to touch and (iv) Ruffini endings exhibit slow adaptation to pressure/temperature. Thus, pressure is the primary transduction mechanism in tactile sensing. Fine-scale textures with roughness less than 200 μm elicit fast responses of the Pacinian receptors (with a spectral resolution of 250 Hz) while coarser textures with roughness exceeding 200 μm elicit moderate responses of the Meissner receptors (with an optimal sensitivity of 50 Hz). Whiskers are an indirect form of tactile sensing - arrays of flexible elastomeric whisker contacts mounted onto pressure/force-sensitive load cells provide a mechanism for tactile sensing [7]. On contact, each whisker bends, the joint angles and forces of which are measured. This may be due to fluid flow, linear acceleration, gyroscopic rotation, etc. Reaction force F and moment N due to tip displacement Δ is given by:

$$F = \frac{3\pi E d^4 \Delta}{64 L^3} \text{ and } N = \frac{3\pi E d^4 \Delta}{64 L^2} \quad [1]$$

where E=whisker Young's modulus, d=whisker diameter, L=whisker length. Whisker sensing represents a universal sensor modality in biological systems for the measurement of a wide range of mechanical effects that may be adapted for a range of applications. An example is a bio-inspired gyroscope based on the haltere organs of the blowfly [8]. Flies are dual-winged insects in which the hind wings comprise a pair of halteres [9]. The halteres oscillate up and down with a frequency of a 150 Hz in antiphase to the wings. At the base of each haltere are 400-500 strain receptors which detect coriolis forces generated by attitude changes.

There are several types of direct tactile deformation sensors which exploit different transduction mechanisms but there are many common features. In the simplest form of tactile sensing, an elastomeric silicone rubber layer (such as PDMS - polydimethylsiloxane) protects an underlying array of embedded force-sensitive sensors. The force/pressure sensors may be formed by the intersections of an orthogonal network of electrically conducting (aluminium) wires. On a variation on this, the meander of a strain gauge may be sandwiched within two prestrained elastomeric silicone rubber substrates [10]. There are other options. Capacitive sensing in a deformable dielectric such as PDMS is given by:

$$F = \frac{CV^2}{2d} \quad [2]$$

where $C = \frac{\varepsilon_0 \varepsilon_r A}{d}$. The piezoresistive effect involves change in electrical resistance in an electrical conductor (such as aluminium) due to applied force altering the dimensions of the conducting element:

$$\frac{\Delta R}{R} = \frac{\Delta L}{L}(1 + 2\nu) + \frac{\Delta \rho}{\rho} \quad [3]$$

where ρ=resistivity, L=length, ν=Poisson's ratio. The piezoresistive element is embedded in flexible polymer such as the PDMS which increases the sensor's sensitivity. Polysiloxanes ($RSiO_{1.5}$) can be transformed into piezoresistive SiOC ceramics through pyrolysis in an inert atmosphere at or above 1400°C yielding an extremely high piezoresistive sensitivity of ~145 [11]. The piezoresistivity of carbon black within the elastomeric silicone rubber gives decreasing electric resistance with increasing applied pressure [12]. The composite resistance is given by:

$$R = \left(\frac{L}{N}\right)\left(\frac{8\pi hs}{3a^2\gamma e^2}\right)e^{\gamma s} \quad [4]$$

where L=number of carbon particles in a single conducting path, N=number of conducting paths, h=Planck's constant, s=silicone insulation thickness between conductive particles, a=effective cross-sectional area, e=electron charge, $\gamma = \frac{4\pi}{h}\sqrt{2m\varphi}$, φ=potential barrier height, m=electron mass. Change in electrical resistance due to applied stress σ is given by:

$$\frac{R(\sigma)}{R(0)} = \left(1-\frac{\sigma}{M}\right)\exp\left\{-\frac{4\pi\sqrt{2m\varphi}}{h}D\left[\left(\frac{\pi}{6\varphi}\right)^{1/3}-1\right]\frac{\sigma}{M}\right\} \quad [5]$$

where D=carbon black particle diameter, φ=particle volume fraction, M=silicone compressive modulus. Strain sensors may be directly fabricated within elastomeric silicone rubber by extruding a viscoelastic ink into a liquid elastomer [13]. The ink comprised carbon black particles suspended in silicone oil forming a resistance filament pattern in the liquid silicone elastomer matrix (ecoflex). However, these methods require carbon for both carbon black and silicone side chains. Although silicones such as PDMS may be manufactured on the Moon in-situ from CO_2 and H_2 derived from volatiles in lunar regolith through the well-established Rochow process (Appendix), such volatiles are scarce.

Piezoelectric materials generate an electric field which alters its resonant frequency in response to mechanical stress or vice versa. The piezoelectric effect involves change in electrical voltage in a piezoelectric element due to an applied stress:

$$D_i = d_{ij}\sigma_j + \varepsilon_{ii}^T E_i = e_{ij}S_j + \varepsilon_{ij}^T E_{ii} \quad [6]$$

where D_i=electrical displacement, σ_{ij}=mechanical stress, ε_{ii}=electrical permittivity, E_i=electric field, S_j=mechanical strain, d_{ij} and e_{ij}=piezoelectric coefficients of a 3x6 piezoelectric matrix. Piezoelectric polymers such as PVDF or Parylene-C may be employed for inertial sensors (accelerometers) and tactile sensors offering compliance within the sensitive material itself [14]. PVDF-trifluoroethylene film on a metal oxide semiconductor field effect transistor with integrated temperature sensors can form tactile sensor arrays [15] but this requires organic piezoelectric materials. A similar problem afflicts the embedding of arrays of organic field effect transistors into elastomeric silicone rubber to measure pressure [16]. Organic thin-film transistors are based primarily on low-temperature p-type semiconductors based on conjugated polymers such as pol(3-hexylthiophene-2,5diyl (P3HT) and 6,13 bis-(trisopropylsilylethynyl) (TIPS)-pentacene but they cannot be 3D printed into fine structures [17. None of these are practically manufacturable on the Moon due to the paucity of carbon.

Elastomeric silicone rubber may be impregnated with microfluidic channels filled with conductive fluid – strain applied to the sensor alters the electrical resistance of the fluid. The conductive fluid may comprise (a) conductive solids as particles or fibres such as carbon black or iron nanoparticles suspended in silicone oil; (b) gallium-indium alloy to form circuits for strain or pressure sensing in artificial skin [18]; (c) electrorheological (ER) or magnetorheological (MR) fluids, i.e. conducting or ferromagnetic particles respectively suspended in silicone oil. Iron and other particles suspended in silicone oil represents a viable option using lunar resources – iron may be extracted from lunar ilmenite (iron-titanium oxide) minerals. ER fluids comprise small solid particles ~0.1-100 μm in size (such as metal oxide, aluminosilicate or silica) in suspension in a low-viscosity non-conducting fluid such as silicone oil. The application of a high electric field ~1-5 kV/mm increases the fluid's viscosity by polarising the particles to form chain like configurations imparting rapid and controllable actuation behaviour [19]. The reverse process provides force sensing capability. Solid particles may be manufactured from lunar mineral resources and silicone rubber/silicone oil is derived from syngas (Appendix).

Lead zirconate titanate (PZT) is the commonest piezoelectric ceramic adopted in engineered systems but there are other ceramic options – berlinite ($AlPO_4$), Rochelle salt ($KNaC_4H_4O_6.4H_2O$), topaz ($Al_2SiO_4)(F,OH)_2$), barium titanate ($BaTiO_3$), lead titanate ($PbTiO_3$), potassium niobate ($KNbO_3$), zinc oxide (ZnO), aluminium nitride (AlN), etc. All ferroelectric materials such as lead zirconate titanate (PZT) are piezoelectric but not vice versa. A piezoelectric material may be formed into semiconducting piezoceramic microwires embedded in an elastomeric silicone rubber to measure strain due to changes in Schottky barrier height at the two ends of the wire [20]. Piezoelectric ceramics may be substituted for piezoelectric polymers offering much higher temperature tolerances and they may be embedded in elastic polymer to permit flexibility. However, these ceramics are rare on the Moon.

The simplest piezoelectric ceramic is quartz (SiO_2). On Earth, quartz is the second most abundant mineral after feldspar as a constituent of granite and the primary mineral of sandstone on Earth. Quartz is however rare on the Moon - mare basalts incorporate only ~6% of relatively pure silica minerals such as cristobalite. However, quartz is manufacturable from lunar silicates as shown in our lunar industrial ecology [3] (Appendix). Quartz may be synthesized artificially in an autoclave through processes developed during World War 2 when Brazilian quartz resources were cut off from the Allies. It involves hydrothermal synthesis of crystals from hot aqueous solution of melted silica below 573°C under very high pressure within a thick-walled steel autoclave pressure vessel sealed with Bridgman seals. A temperature gradient is maintained with the hotter end dissolving the quartz and the cooler end precipitating

the growing crystals to ensure that the quartz is in a supersaturated state. Quartz may be employed as a sensor to measure force or pressure or as an actuator to generate very high frequency oscillation in radiofrequency circuitry. Quartz is ideal as a radiofrequency crystal oscillator – the Pierce oscillator may be constructed with a minimum number of components – one inverter, two resistors, two capacitors and one quartz crystal. Piezoelectric tactile sensors in conjunction with pressure sensors with a feedback circuit can provide sensitive tactile measurements including differentiating between hard and soft objects [21]. An oscillating phase shift circuit allows extraction of the phase shift of the resonance. Quartz constitutes the sensor element to the quartz microbalance (QMB) for the precise and accurate measurement of mass. All pyroelectric materials are piezoelectric including quartz which is sensitive to infrared radiation in which polarisation change is proportional to temperature change [22]. Piezoelectric sensors are sensitive but they cannot measure static forces. Shape memory alloys such as NiTi introduce the possibility of shape memory actuation based on temperature or vice versa. Temperature is a fundamental measurement that is essential for temperature compensation as part of general signal processing (typically implemented through a bridge circuit).

Tactility is fundamentally an actuator-driven sensory modality as touch is exploratory. Sliding motion generates ~micron amplitude vibration ~200 Hz (similar to Pacinian corpuscle responses) that correlate with textural roughness. Because this process is iterative, it is amenable to Bayesian treatment [23]. Complex motor activity is required to measure force distribution for the construction of tactile "image" maps (arrays of taxels). It is essential that the 3D location of the skin taxels are calibrated with respect to a central reference frame through maximum likelihood mapping [24]. Edge and line detection algorithms such as the Hough transform may be applied for the extraction of basic tactile properties - contact area, centroid estimation, eccentricity and principal axis determination may be computed using tactile moments. However, tactile data is noisy requiring the use of sophisticated filtering methods and artificial skins tend to exhibit poor wear and tear tolerance. A key lesson is to implement actuation as a key component to sensation. Actuation in elastomeric materials adopted in sensing offers distinctive actuation capabilities. The Venus flytrap is a carnivorous plant that snaps shut its hinged lobes to trap its insect prey. The flytrap can actuate faster than hydraulic transmission by virtue of its pre-stressed lobes buckling between two mechanically stable states [25].

III. PHOTOMULTIPLIER TUBE (PMT)

Simple proximity sensing is feasible using a simple metal detector comprising an oscillator circuit that generates an AC through a coil generating an alternating magnetic field at frequencies of 5-20 kHz. Nearby electrically conductive metal close to the coil experiences eddy currents that generate their own magnetic field. Another coil acts as a magnetometer to detect this change in magnetic field. However, long-range sensing using cameras are essential in spacecraft and rover operations - they are versatile in their application. The Visual Monitoring Camera (VMC) on Mars Express evolved from its original role to provide visual feedback of the separation of the Beagle 2 lander from the Mars Express orbiter to imaging the Martian surface during the orbital mission [26]. Such VMC are useful for monitoring mechanical deployments on spacecraft rather than relying on indirect measurements (e.g. Galileo antenna deployment). The 16 kg 35 cm diameter AERCam (autonomous EVA robotic camera) Sprint flew on STS-87 (1997) as a freeflying camera teleoperated through a translational/rotational hand controller to support astronaut operations. The dual-camera system used 12 nitrogen gas thrusters and angular rate gyros for attitude control under microgravity. A 5 kg 19 cm diameter nanosatellite class version – mini-AERCam – had three CMOS imaging array cameras with lights supported by two GPS antennas to provide self-localisation with onboard micro-gyroscopes [27]. These cameras set a precedent for the implementation of mobile remote camera observation to support astronaut activities on the International Space Station. We would expect this to continue to support astronaut operations on the Moon. This extends to robotic operations including the construction of infrastructure - imaging cameras are essential for robotic operations as the main primary sensing-at-a-distance modality.

Visual imaging begins with a set of radiance measurements at each photoreceptor of an array of pixels. We first consider a single pixel. There are several approaches to photosensitivity, the most mature being photovoltaics. However, the requirement for precise doping to form pn junctions would be challenging under lunar conditions [28,29]. Colloidal semiconducting quantum dots are fluorescent semiconducting nanocrystals <20 nm diameter comprising an inorganic core (such as $CdSe/TiO_2$) surrounded by organic ligand shell (such as PMMA) synthesised through wet chemistry [30,31]. Quantum confinement within the quantum dot provides tailorable quantised energy levels and optical properties but photovoltaic efficiencies are currently low ~7% [32]. This is not feasible on the Moon due to the challenges in sourcing and extracting Cd and organic material (though TiO_2 is extractible from lunar ilmenite).

Photomultiplier tubes (PMT) are vacuum tubes that operate through the photoelectric effect rather than thermionic emission [33]. As vacuum tubes, PMTs are constructed from a glass envelope enclosing a high vacuum within which a photocathode and anode sandwich a series of dynodes (Fig 1).

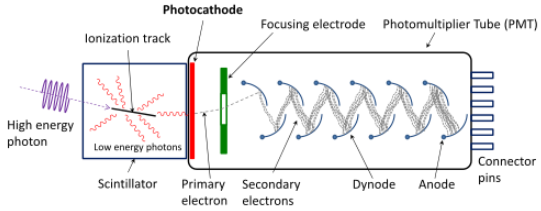

Fig 1. Photomultiplier tube

The window may be transparent fused silica glass (derivable from lunar silicates - Appendix) which is transparent to UV radiation down to 160 nm wavelength. The glass window focusses light onto the photoemissive cathode which, through the photoelectric effect, emits electrons into the vacuum. The photoelectrons are accelerated by a focussing electrode onto the series of dynodes (nominally 9-12 stages) which act as electron multipliers through secondary electron emission. Each dynode is held at a more positive voltage ~100 V to attract the electrons in one direction and add ~100 keV of energy at each stage. By the time they have reached the anode over 1-2 kV, an avalanche current is generated. After a series of such electron multiplications at higher electrical potentials, $x10^8$ amplified electrons are collected by the anode positioned very close to the last dynode. The quantum efficiency is the ratio of output electrons to input photons:

$$\eta = (1-R)\frac{P_v}{k}\left(\frac{P_s}{1+1/kL}\right) \quad [7]$$

where R=reflection coefficient, k=absorption coefficient of photons, P_v=probability that light absorption excites electrons to escape, L=mean escape length, P_s=probability that electrons are released from dynodes. Photoelectron emission occurs if incident photons exceed a critical energy threshold (work function plus valence-conduction bandgap). The key is the photocathode material which is typically an alkali metal or III-IV semiconductor and the dynode comprising secondary electron emitters which eject electrons exceeding the Fermi level and work function >10 eV. Commonly used photoelectric materials - Cs_3Sb for visible and Na-K-Sb-Cs for UV to NIR response – cannot be readily manufactured from lunar resources. Crystalline silicon cannot be employed as a photosensitive transducer without dopants because of its indirect bandgap. Photocathodes may be alkali metal with low work function such as a thin layer of K coated onto a W metal substrate – K has a work function of 2 eV. Metallic aluminium with a work function of 4.08 eV in transmission mode photocathodes requires very thin layers ~20 nm [34]. The electron microscope is a PMT-based vacuum tube. An electron gun accelerates the electrons to ~kV directed by a magnetic focussing lens and a magnetic objective lens into a narrow beam ~10 nm in diameter. A metal-coated sample is irradiated with an electron beam scanned over the sample surface using a pair of focussing magnetic lenses. The metal-coated surface generates secondary electrons which may be detected with the dynodes of a PMT array.

High resolution imaging may be feasible with an Al/TiO_2 junction, both common resources on the Moon. A rectenna (rectifying antenna) converts an AC input to a DC output using a diode clamping circuit followed by a DC smoothing pass filter. The antenna must be comparable in size to the wavelength of incident radiation so higher frequency requires smaller antenna. However, efficiency of the rectenna drops with increasing frequency with >90% at 2.45 GHz to 60-85% at 5.8 GHz reaching sub-1% efficiencies in the visible spectrum. This problem may be circumvented through the exploitation of plasmon resonance at visible wavelengths. The rectenna can be operated at high frequencies up to ~THz including visible light in which the antenna is an array of half-wave nanodipoles [35]. Higher efficiency results from hot electron emission from plasmonic nanostructures due to surface plasmon resonance [36]. This is caused by confined free electrons oscillating with the same frequency as incident light $w_{SPR} = \sqrt{\frac{ne^2}{3m\varepsilon_0}}$ due to nanostructured metal (such as Al for 400-600 nm spectral region) on an n-type TiO_2 semiconductor (ΔE=3.3 eV) substrate where n=carrier concentration, m=electron mass, e=electronic charge. Conversion efficiency is close to 50% for multispectral light. The metal nanostructures (such as nanorod arrays) act as nanoantennas that generate surface plasmons which decay from which the plasmon resonance energy is transferred to the semiconductor conduction band by hot electrons generating a photocurrent over the Schottky barrier [37]. Multiple nanoantenna arrays with different resonant frequencies offer the potential for spectroscopy. Electron beam lithography deploys an electron beam to pattern nano-structures with sub-10 nm resolution. An electron beam is generated from an electron emission source shaped and focussed by a series of electromagnetic lenses. However, it is not clear that electron beam lithography is feasible as an in-situ lunar manufacturing technology.

For optical sensitivity, rather than using junction materials which will be difficult to manufacture with precision on the Moon (such as through the microwave applicator [38], we have chosen the simplest light-sensitive material – selenium – as the photocathode that was used in Alexander Graham Bell's photophone. Amorphous selenium powder as a photocathode is a p-

type semiconductor with an optical energy gap of 1.99 eV [39,40]. The photoelectric current is given by Fowler's law: $i = k(h\upsilon - \phi)^n$ where k=constant, n=material exponent. On Earth, selenium is found in minerals eucairite (CuAgSe), crooksite (CuThSe) and clausthalite (PbSe) in metal sulphide ores. Most selenium on Earth is extracted as a byproduct of electrolytic refining of chalcopyrite (CuFeS) deposits (with Se substitution of S) which do exist on the Moon but are rare. Despite its name, selenium is rare on the Moon though it occurs in meteorites in approximately constant Se/Te abundance ratios of ~10-20 by weight, the Se content varying from 0.5-10 ppm [41]. In carbonaceous chondrites, Se is in found in association with the 2500 times more abundant S such as found in troilite (FeS). Troilite is common in iron meteorites and occurs in association with graphite grains in irons. Selenium may be extracted through treatment with HF/HNO_3 digestion in the presence of alumina (Al_2O_3) followed by purification with the organic reagent ascorbic acid [42] but organic acids are impractical on the Moon. Following a similar treatment to copper selenide, a troilite source of FeSe may be smelted with soda Na_2CO_3 in solution using a saltpetre KNO_3 catalyst:

$FeSe + Na_2CO_3 + 1.5O_2 \rightarrow FeO + Na_2SeO_3 + CO_2$

Saltpetre could be manufactured from KREEP minerals and nitrogenous lunar volatiles (it may also be used for blasting as saltpetre mixed with sulphur and charcoal forms the basis of gunpowder). Lunar orthoclase offers a more practical source (Appendix). Selenite Na_2SeO_3 may be acidified with H_2SO_4 yielding selenous acid (H_2SeO_3) from which Se may be precipitated:

$Na_2SeO_3 + 2H_2SO_4 \rightarrow$

$H_2SeO_3 + Na_2O + 2SO_2 + H_2O \rightarrow$

$Na_2O + 2H_2SO_4 + Se$

The sulphuric acid reagent is thus recycled. Treatment of troilite (FeS) in the presence of H_2S in aqueous solution yields iron pyrite (FeS_2) with the evolution of hydrogen, the rate of reaction increasing with temperature up to 125°C [43] – indeed, the equivalent transformation at low temperatures have been invoked as part of a biotic redox couple in the iron-sulphur world of early Earth [44]. Iron pyrite FeS_2 offers the possibility of infrared sensitivity. Thin FeS_2 pyrite films ~μm are n-type semiconductors that exhibit photoconductivity with high absorption coefficient $\alpha > 5x10^5$/cm for $\lambda < 900$ nm and bandgap $E_g = 0.95$ eV [45]. The question of manufacturing thin films by chemical vapour deposition on the Moon however remain open.

Secondary electron emitters are typically alkali metal oxides such as Al_2O_3 or MgO coatings on nickel, aluminium or steel dynodes [46] though any alkali metal oxide (e.g. CaO or K_2O) will have secondary electron emission properties. All these oxides are extractible from lunar resources as outlined in our lunar industrial ecology [3] (Appendix). The number of secondary electrons emitted per incident electron is typically ~4-6 for a few hundred volts. Stray magnetic fields can be controlled using permalloy (80% nickel-20% iron alloy) manufacturable from lunar resources.

PMTs are highly sensitive optical detectors with high signal-to-noise ratio that may be arrayed into pixels in a microchannel plate, a thin parallel array of glass channels, each acting as an electron multiplier. The microchannel plate comprises a regular array of tiny tubes ~10 μm in diameter spaced ~15 μm apart separated by electrically resistive walls. These glass walls act as continuous dynode electron multipliers onto which a photon strikes causing a cascade of electrons. They use a strong electric field to accelerate the electrons through each channel amplifying the incident signal by many orders of magnitude. The PMT may be deployed as a mobile camera.

IV. LIDAR

What about leveraging optical laser technology on the Moon? LIDAR has applications in depth measurement for visual mapping of the environment. The laser comprises a pumped energy source, a lasing medium and an optical Fabry-Perot resonator. The optical cavity resonator comprises two parallel mirrors, one fully reflective and the other partially reflective to amplify light intensity through stimulated emission. The lasing medium provides optical gain that amplifies light input by stimulated emission. An optical pump supplies the input energy and an optical feedback mechanism is enabled by the optical cavity formed by the pair of mirrors. The optical pump is typically a noble gas flashtube for generating population inversion in the lasing medium. Stimulated emission results from oscillating light between the two mirrors which must be polished and flat to within λ/4. The Townes maser (microwave amplification by stimulated emission of radiation) preceded the Maiman ruby laser (light amplification by stimulated emission of radiation) [47] illustrating that non-visible light can be amplified at a single wavelength. The simplest form of laser uses a high-pressure nitrogen (or air) gas medium which has such a high gain of 2 that mirrors are not required. However, the lasing is self-limiting - a 100 kW UV-A pulse at 337 nm is generated and decays within nanoseconds of the initiating discharge. A reflective rear mirror doubles its power output. It cannot be readily focused making it useless for material processing but it may be used to pump a dye laser. Dye lasers are relatively simple to construct using a nitrogen laser pump with fully reflective rear mirrors. Pulsed lasers are more readily built with lower reflectivity mirrors (~80% reflectivity is readily achievable with polished Al) than

continuous wave lasers which require ~99% reflective dielectric mirrors. However, they are based on organic media which are rare on the Moon as is nitrogen. A high-powered Hg UV discharge lamp can be substituted for a UV laser, useful for UV photolithography. A simple laser may be constructed but the discharge lamp requires a high voltage of 20 kVdc which can be achieved with a Blumlein circuit. However, Hg is not readily available on the Moon.

Optical fibres are silica glass - fused silica glass is manufactured by melting silica (derived from lunar silicates) at ~2000ºC in a furnace. It can then be seeded in sodium silicate at 350ºC and 150 bar (Appendix). It is plausible that metallic cladding of nickel or cobalt might be employed to generate internal reflection within the glass fibre core rather than graded doping of glass cladding [48]. Optical fibres may replace conducting wires in the elastomeric silicone rubber to measure changes in optical transmission under strain. Optical fibre tactile sensing relies on modification of parameters of transmitted light such as intensity through an optical fibre due to an applied force. Amplification of light signals within an optical fibre may be achieved by doping the silica of the fibre by the rare earth element erbium. This can be pumped by a diode laser to emit stimulated photons at higher power. The use of chalcogenide glasses containing elements from group 16 (such as S) allows the fibre to act as a resonating cavity. Application to photonic materials offers the possibility of switching with chalcogenides. However, most solid-state and optical fibre lasers are based on crystal or glass rods which are doped with rare-earth elements such as Nd (as in Nd:YAG) or Ti (as in Ti:sapphire) pumped by flash lamps or doped semiconductors (based on III-V junctions). Ti is available on the Moon and Al_2O_3 can be extracted from lunar minerals as corundum - synthetic sapphire (Co-doped corundum) may be manufactured through the Czochralski process, hydrothermal synthesis or the Verneuil flame process. Similarly, synthetic ruby (Cr-doped corundum) can be manufactured – ruby lasers are the most viable option. Rubies can be synthesized from a mixture of Al_2O_3 and Cr_2O_3 powder heated to 2000ºC in a hydrogen-oxygen torch followed by seeding growth in sodium carbonate at 445ºC and 380 MPa [49]. Ruby lasers were the first (Maimon) lasers and output 1 kW power at 694.3 nm (red). The rod ends are polished flat and parallel within λ/4 and silvered to create the Fabry-Perot etalon. Despite its low efficiency and low repetition rate, ruby lasers are commonly used for drilling holes in diamond, illustrating their utility in material machining. Solid-state diode laser pumping such as Nd:YAG offers high efficiencies up to 50% but optical pumping with flashlamps or other lasers is typically inefficient ~2%. Nd:YAG continuous lasers are the best solid-state lasers at 1.06 μm but rare earth materials are difficult to extract from lunar resources. The short pulse Ti-doped sapphire (Al_2O_3) laser is tunable across 660-1180 nm but requires diode laser pumping. Electron beam pumping has been applied to excited dimer (excimer) lasers such as KrF lasers at 259 nm but Kr and F are highly rarified on the Moon. Electron beam pumping through wiggler magnets is the basis of the free electron laser (FEL) tunable from microwave to X-ray but a powerful electron accelerator is required [50]. The CO_2 gas pulsed laser pumped by electrical discharge outputs 25 kW power output at 10.6 μm but increased efficiency to 10% requires the addition of helium. Both carbon and helium volatiles are scarcer on the Moon than mineral resources. We thus conclude that lasers cannot be readily manufactured from lunar resources for first generation ISRU capabilities due to the stringent manufacturing techniques, required stringent tolerances of λ/4 and marginal accessibility of functional materials.

V. BIOINSPIRED VISION

Classical image processing assumes large arrays of pixels and is computationally intensive which is not suited to small PMT arrays. As explained later, we have adopted neural network architectures for computation. We shall briefly explore biological vision to determine if we can exploit bio-inspired approaches to robotic vision to compensate for the challenges imposed by lunar-derived imaging technology. In animals, the eye has been estimated to have evolved rapidly and independently from a lenseless patch of simple light-sensitive cells in an eyecup in Cambrian molluscs, arthropods and chordates into eight basic optical designs with graded refractive index lenses, testament to the importance of biological vision [51,52]. Human visual processing is a multi-stage process (simplified here to its bare essence) involving centre-surround neurons that is dedicated towards motor action [53]: (i) LGN (lateral geniculate nuclei) extracts primary colours (red, green and blue); (ii) V1 extracts edges at different orientations through Laplacian filters (good approximation of the stationary autocorrelation matrix of the image) while V2 extracts texture using Gabor wavelets (a windowed Fourier transform); (iii) V2-V4 forms the ventral pathway to extract visual features generated by active contour (snake) models while V2-MT (middle temporal) forms the dorsal pathway that uses optic flow to extract motion; (iv) ventral pathway IT (inferior temporal) performs object recognition in a winner-takes-all process; (v) dorsal pathway MST (medial superior temporal) performs optic flow of global motion including self-motion; (vi) IP (intraparietal) receives both streams and integrates them into a salience map of the visual field for generating oculomotor commands by the premotor cortex. The convolutional neural network emulates the biological architecture by extracting simple

visual features that are then linked by successive layers to construct more complex features.

Detection of visual motion requires detection of retinal slip of visual features in V1 followed by selective integration of those moving features through a correlation algorithm implemented in the MT, i.e. optic flow field [54,55]. The correlation algorithm is realized as directionally-sensitive delayed inhibition between neighbouring pixels. In motion sensitive neurons, velocity of motion is encoded in neural spike timing [56]. Hence, optic flow is fundamental to visual perception of a dynamic world. The primate visual cortex (around 25% of the human cortex) exhibits a network of feedforward, feedback and lateral corticocortical pathways [57,58], e.g. V1 projects to V2 which reciprocally projects back to V1. There is information flow in both directions in which hypotheses influences data (Bayesian framework) combining bottom-up and top-down information flows. The primate visual processing system represents a deep hierarchy of up to 10 levels of hierarchical and parallel cortical processing [59]. Human motor response to visual stimuli takes 400-500 ms suggesting that each neuronal stage takes 20-30 ms per synapse [60]. V1 response occurs at 40 ms then most of the visual cortex has responded by 80 ms and then at 120 ms motor cortex response begins. Neural discharge in a population of neurons - assumed to correlate with an observable cognitive behaviour - is often subject to a delay in response time ~100 ms. At each stage of the feedforward pathway, recurrent feedback is activated to modulate earlier processing. Recurrent feedback activity is essential for visual awareness which in turn must be action-oriented with respect to motor acts and general active exploratory behaviour [61,62].

There are two visual processing streams in the visual cortex with little cross-talk between them: the ventral (occipitotemporal) P pathway (V1-V2-V4-IT) is concerned with object identification (what) while the dorsal (occipitoparietal) M pathway (V1-V2-V3-MT/MST) is concerned with spatial and motion relationships of objects (where) [63]. The latter pathway V1-MT/MST acts as a saliency map. Visual information is selectively processed for the spotlight of attention (visual awareness) in working memory. Attention is directed to objects of high behavioural relevance as indicated by the well-known change blindness phenomenon. Vision involves a bottom-up stimulus-driven dorsal (where) pathway that selects targets on the basis of saliency dictated by centre-surround processing (to detect perceptual figure/ground Mexican hat contrast) at multiple scales (using a Gaussian pyramid of 2D difference-of-Gaussian filters) of basic visual properties (such as intensity, colour, orientation, motion, etc) by forming a topographic saliency map [64]. Saliency of stimuli depends on its contrast with the surrounding context. A top-down hypothesis-driven ventral (what) pathway provides feedback by modulating the visual targets on the basis of behavioral importance, i.e. object recognition [65]. The saliency map is a unique 2D map encoding saliency (or noticeability) of objects in the visual environment constructed bottom-up. The saliency map is constructed from information from multiple modalities which are combined into the saliency map. A multiresolution convolutional neural network can use local contrast, global contrast and other top-down visual factors as saliency cues from image inputs to predict eye fixations [66]. The saliency map may be represented as a topologically local neighbourhood map in which an information maximum metric predicts eye fixation locations [67]. There are multiple visual objects in visual locations encoded by integrate-and-fire neurons which compete through a neural winner-take-all algorithm to be the next visual target of saccadic eye movements and/or focus of attention [65]. The winning neurons are subsequently inhibited (inhibition of return which acts as a memory mechanism) so that the focus of attention is directed to the next most salient location. Selection of gaze fixation positions is effectively Bayesian in updating top-down (prior) hypotheses with new visual data. Action-directed eye movements provides the basis for active vision.

The pulvinar nucleus of the thalamus may implement control neurons that direct attention through the “what” pathway on receiving input from a saliency map of the “where” pathway via corticocortical pathways [68]. A Y-shaped what-where (ventral-dorsal) bidirectional network has demonstrated integration of bottom-up visual data-driven processing and top-down motor-driven processing [69]. Top-down signals propagate motor representations through both pathways. Neural fields that learn through a random motor babbling implement rapid learning of mappings between retinal image space of the eye and the six-eye muscle motor space to control visual saccades [70]. Interaction with the environment provides the opportunity to learn mappings of visual features into actions [71]. Such a visual control policy can be learned through reinforcement preceded by a Markovian visual classifier, e.g. temporal difference algorithm. It appears that it is more efficient to extract and process different visual properties independently and in parallel before being bound by synchronous firing at higher processing levels. A similar division occurs in auditory cortex with a “what” stream and a “where” stream subsequently exploited in spoken language to distinguish spoken message from speaker [72,73]. This reinforces the evidence that sensory data should be partitioned into independent processing streams.

We adopt a bio-inspired appoach to vision suited to the small PMT arrays. We separate our active vision

(what) pathway for object identification and our optic flow (where) pathway for navigation.

VI. ACTIVE VISION

We expect the imaging resolutions of in-situ manufactured imagers using small array PMT pixels to be poor but we can learn from biomimetics to compensate. Active vision exploits actuator-driven exploration of the visual field to minimise imaging pixel hardware. The human eye is characterised by a large concentration of $7x10^6$ cones with a density of 5000 cones/μm within the ±0.5-1.0° foveal region of the retinal array about 5° off the optic axis for high resolution imaging [74]. The blindspot itself ~5° in size where the retina feeds into the optic nerve is invisible to perception. Away from the fovea, the distribution of the other 120 x 10^6 visual receptors becomes more diffuse with lower resolution throughout the majority of the visual field. Around 50% of the visual cortex is devoted to processing foveal data.

Gaze shifting and gaze holding movements of the eye provide a means to rapidly aim this narrow field of view (FOV) – this is central to active vision [75]. Fast saccadic eye movements move the fovea between different targets in the visual field while active gaze control keeps the fovea on a specific target (visual fixations). Between fixations, saccades direct the fovea onto targets in the visual field. They are point-to-point movements of the eyes at 900°/s which bring the high-resolution fovea to visual targets at a rate of 2-3 Hz, each fixation being ~30 ms in duration - we make ~100,000 searches per day. Each saccade yields discontinuous changes in retinal motion and alters retinal projection of the heading direction. The saccades rapidly shift gaze over the visual field under the control of a neural circuit involving the frontal lobe, basal ganglia, cerebellum and superior colliculus. Tracking is updated with every saccade which changes the direction of motion with every saccade. This is a Bayesian approach in which the posterior likelihood is the prior likelihood updated by the latest fixation [76]. Selection of viewpoints for gazing in active vision may follow a gradient $\frac{\partial \sigma^2}{\partial x}$ of prediction variance σ to reduce uncertainty [77]. A neural integrator maintains an equilibrated eye position during visual fixation between saccades [78]. The superior colliculus represents a topographic map of saccade vector fields which may be represented by a neural network with an upper layer connected to the lower layer by feedforward connections with weights determined by a recurrent backpropagation algorithm [79]. Reciprocal inhibition of gaze-shifting neurons and gaze-holding neurons in the superior colliculus determines which neurons are active. Saccade termination is driven by the error between current eye position and desired eye position which influences neuronal discharge rates [80]. Discharge rates are modulated through the time delay inherent in reaction times [81].

Active vision reduces the requirement for optical hardware by actively orienting a high-resolution fovea over the visual field. We may exploit such active vision in engineered cameras to accommodate limited FOV. In engineered active vision, the camera is mounted onto a pan-tilt unit to permit slewing of the camera illustrating an example of Gibsonian affordances. Gibsonian affordances are the potentials for action afforded by the properties of the environment (objects, events and locations) relative to the agent [82]. The effectors are then actuated to realize a specific affordance. Such slewing is implemented by electric motors with feedback from rotary potentiometers on motor position at each motorised joint. The extended Kalman filter augmented by iterative adaptation may be applied to the dynamics of this visual servoing [83].

There are two options for feedback on camera slewing – optical and vestibular. Optic flow consists of a flowfield in which all motion is directed away from the focus of expansion to indicate heading. Eye movements with respect to the body introduce an additional retinal image motion which is superimposed on the optic flowfield. The direction of eye movement required to stabilize gaze on the target occurs along a flowline away from the heading point. Eye rotations shift the focus of expansion by $(d/x)\theta$ where d=distance of place from observer, θ=rotation of observer, x=translation of observer. Hence, optic flow involves using eye movements to track retinal motion in the direction of gaze. Although direct visual estimation of movement through optic flow is adequate for slow eye movements <1.5°/s (optokinetic response), at higher speeds, non-visual information is required, i.e. vestibular information through the vestibular ocular reflex (VOR). The unscented Kalman filter has been shown to be effective in implementing VOR-inspired visual servoing [84]. VOR is a reflex that stabilises images on the retina through compensatory eye movements during head movements detected by the semicircular canals. The signal from semicircular canals to the eye muscles is rapidly transmitted through a three-neuron arc with a resulting lag of only 10 ms. VOR (and other widespread neural functions) is a neural feedback system that is subject to gain adaptation through learning that permits integration of multiple information sources [125,85]. However, implementation of inertial measurement on the camera assembly itself is not commonly adopted in robotic systems. Taking a biomimetic stance, the only feedback we have is from the joints of the camera mast/pan-tilt unit. In mammalian biology, feedback from muscles is generated by the spindles (position-derivative) and Golgi tendon sensors (force) which provides local

muscular force feedback to orient the eyes. To compensate for this reduced observability, predictive feedforward control (implemented by a pre-trained neural network) may augment feedback to provide robust estimation of visual tracking (Fig 2) [86].

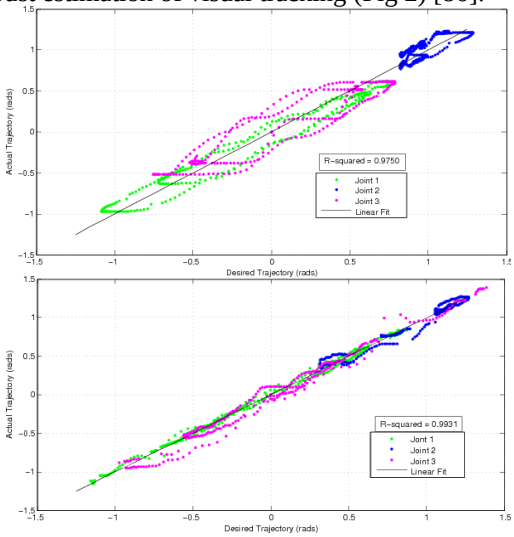

Fig 2. Error excursion for a 3 degree-of-freedom camera mast (a) feedback only (b) feedforward-augmented feedback

This demonstrates how forward modelling using neural networks may be employed to enhance feedback from position sensors (such as rotary potentiometers) in camera pointing. This is also required in a three-component system for accurate tracking in smooth pursuit: a feedback controller (subject to significant delays), target velocity predictive controller and an inverse oculomotor model [87]. A feedback error learning controller uses the output of the PD feedback pathway as a teacher signal to improve the performance of VOR.

Motor control of the camera is central to active vision. Motorised micro-stepping offers the potential for circumventing resolution limits in PMT arrays. We have demonstrated how electric motors may be potentially 3D printed from lunar resources [88]. Our prototype 3D printed motor was printed using Proto-Pasta comprising 50% iron particles embedded in a 50% PLA (polylactic acid) matrix by weight offering a soft magnetic medium (Fig 3). Both the closed magnetic circuit stator and the rotor were constructed from Proto-Pasta with copper wire windings to create a fixed electromagnet (stator) and alternating electromagnet (rotor). A 3D printed lunar variant could be replaced with either abundant nanophase-iron impregnated lunar glass or iron particle-impregnated fused silica glass for the stator/rotor and copper windings with aluminium windings.

Fig 3. 3D printed electric motor

Such motors would be the primary mechanism for implementing active vision. The feedback control of the joints using rotary potentiometers should offer higher resolution of control than the PMT pixel resolution allowing the camera to orient over the visual field with higher than pixel resolution. A stepper motor variant of a 3D printed motor can potentially improve this resolution further by implementing micro-stepping.

VII. OPTIC FLOW VISION

Whereas active vision is associated with object identification, optic flow may be associated with visual navigation. Optic flow is fundamental to vision - even during fixated visual gazing there are small involuntary microsaccades ~arcminutes in amplitude with ~0.6 s periods. This is required to maintain permanent vision – complete immobolisation of the eyeball causes objects to disappear. The eye detects intensity fluctuations over time measured by the retina rather than absolute intensity as the latter would yield visual artefacts such as blood vessel shadows, etc. Gibsonian ecological perception suggests that physical laws and ecological constraints of the environment limits possible interpretations of sensory stimuli [82]. The stimulus information is encoded as invariants which specify environmental properties. Optic flow is such an affordance that provides for direct motor control with minimal requirement for inferential processing [89].

Honeybees have small brains (~960,000 neurons with a 1 mm^3 volume) with a modular construction with independent sensorimotor functions [90]. There is horizontal (central) integration but visual, mechanosensory and olfactory information appears to occur in the mushroom bodies, each comprising ~170,000 tightly-packaged neurons [91]. Insects possess eyes of fixed orientation and fixed focus and cannot use binocular stereopsis for depth estimation due to the small baseline between the two eyes. When an insect moves, optic flow generates information on the motion

of the animal as well as objects in the environment. Insects lack a visual cortex possessing a brain of only ~10^6 neurons and perform only low-level visuomotor processing. A low pass Gaussian filter provides spatial filtering at the photoreceptors while predictive coding provides temporal high pass filtering. The eye of Drosophila melanogaster comprises 700 omnatidiae backed by three neural layers – neuropils lamina, medulla, and lobula complex – which perform contrast enhancement, signal amplification and motion detection. The insect compound eye comprises arrays of low resolution ommatidia connected to an analogue neural network with overlapping Gaussian receptive fields of view but with variable spatial acuity over the eye [92]. Ommatidia form groups with a central pixel surrounded by six neighbouring pixels and it is the overlapping Gaussian response of the ommatidia that renders its superior performance. Motion is detected by comparing visual signals in a small patch of the visual field with delayed signals in neighbouring patches.

An elementary motion detector generates the strongest response when the visual pattern moves in a specific direction (Reichardt detector) [93]. Reichardt detector coincidence between adjacent pixels can be implemented through temporal filtering of the inputs. Insect-inspired vision sensor offers superior performance in rapid but reliable mobile object detection compared to a CCD camera [94]. Insects use image motion to estimate range - when an insect moves in a straight line, the image of a nearer object moves faster than further objects. The distance may be measured by integrating image motion over time (optic flow). Optic flow due to translation induces motion parallax such that optic flow is inversely proportional to distance. This gives a basis for recovering depth information in cues. Rotation generates equal angular motion at all distances. Hence, translation and rotation motion can be distinguished if a minimum of six points can be tracked. Thus rotation-independent, the local motion parallax field allows recovery of the focus of expansion. Optic flow speed is used to determine object distances. Flying insects maintain equidistance between obstacles by balancing the angular speeds of retinal images in the two eyes. Some insects invoke self-motion for the purpose of generating optic flow information from the visual feedback [95,96]. Initial visual processing in flying insects occurs through a 2D array of 48,000 photoreceptors to construct 3000 pixels per eye with 8 receptors/pixel with coaxial receptive fields. This allows optic flow to implement autonomous navigation based on motion detection that may be measured using arrays of analogue elementary motion detectors as a model of insect compound eyes of 3000 pixels [97]. Between neighbouring facets, object velocities are detected to generate a map of obstacles in polar coordinates in eye-centred reference frames. The multi-faceted insect compound eye has been emulated with a 118-pixel model with a concurrent analogue array of 100 Reichardt detectors on a mobile robot [98]. Motion is detected by comparing visual signals in a small patch of the visual field with delayed signals in neighbouring patches. A PI controller can emulate the summation process of neighbouring neurons [99]. Optic flow illustrates an alternative approach to visual navigation based on simple electronic circuitry rather than complex software.

VIII. NEURAL NETWORK-BASED VISION

Neural network architecture offers advantages of reduced physical footprint over CPU-based architectures [100] and are Turing-complete [101]. Neural networks are highly suited to the implementation of both active vision and visual navigation. The pulse-coupled neural network (PCNN) can select visual targets for automated foveation as the key to active vision from a filtered image input [102]. The filtered image may be an optic flow field or edge-filtered image. PCNN divides a receptive field input into two channels - a linking channel that receives local stimuli and a feeding channel that receives external and local stimuli. Linking modulation feeds back the output from the linking channel, applies a threshold and multiplies this with the output of the feeding channel to determine neuronal internal states. A sigmoidal pulse generator fires if it exceeds the threshold which itself is set by a general exponential decay against previous firings which raise the threshold. It is the firings that select the foveation points. Neural networks may represent neural fields by correlating agent motion with a heading direction and velocity as control variables while the environment is characterised by multiple goal heading directions ψ_{tgt} and multiple obstacle heading directions ψ_{obs} relative to allocentric reference coordinates [103,104]. Coupled sets of neural fields representative of different neuronal populations can implement goal-directed behavior [105]. ALVINN (autonomous land vehicle in a neural network) adopted a fully-connected neural network with 30 x 32 visual input nodes feeding into 5 hidden nodes which projected into 30 steering angle output nodes [106]. It implemented a receptive field-based activation distribution in which neurons of a radial basis function respond selectively to spatial or angular position:

$$y_i = \frac{\sum w_{ij}\theta_j}{\sum \theta_j} \quad [8]$$

where $\theta_j = exp\left(\frac{d^2}{b_i^2}\right)$=hidden neuron activation, d=Euclidean distance between neuron centre to input vector, b_i=receptive field width. Neural network outputs can be correlated with sensory visual inputs to construct a vector flow field of the rover rφ in its environment [107].

The two processing streams may be integrated using noise-tolerant neural networks. by emulating the function of the middle temporal (MT) and medial superior temporal (MST) areas of the primate visual cortex. Neural networks may be used to transform optic flow and eye position information into map representations of heading direction, range and location of objects in the scene [108]. The heading network is embedded in the larger network encoding the environment. The self-organising map may then be used to navigate in pursuit of a moving target whilst avoiding obstacles. The primary problem is to separate optic flow generated by eye movement which corrupts the optic flow pattern generated by objects in the scene due to pure translation motion. Neural network weights were trained using optic flow information correlated with eye movements and optic flow information correlated with object movements. Each input neuron is sensitive to a specific optic flow direction given by: $x_i = vcos\phi_i$. Inhibitory connections from pitch and yaw eye velocity neurons ensure cancellation of flow field components due to eye movements. Weight learning is given by: $\frac{dw_{ijk}}{dt} = \eta w_{ik} x_j$ which becomes zero when inputs are equal indicating eye movement compensation. The remaining flowfield components correlate to observer translational velocity. The heading map comprises a topographical self-organising map of cells which receive weighted excitatory inputs from the optic flowfield. The heading cells spread out in different heading directions – the angular separation of neighbouring cells being dependent on the number of cells in the map. Optic flow can also provide depth information by computation of time-to-collision to obstacles. Translational flow speed is logarithmically compressed prior to input to a retinoptically organized depth map of ranges to objects which affords higher resolution to nearby objects.

More complex image processing tasks may be implemented with neural networks. The fundamental process for initial texture analysis is the Gabor transform at different orientations. The Gabor filter is the product of a 2D Gaussian modulated by a complex exponential function that captures local structure including both edges and texture that is invariant to translation, rotation and dilation [109]. Texture analysis proceeds beyond feature extraction – it is concerned with micro-features. A popular approach is to implement Gabor filters in a neural network. A 2D image is presented to the input layer of a neural network where it is convolved with a Gabor filter prior to processing with the classifier segment of the neural network's hidden layer [110]. Prior application with principal components analysis to the image reduces the dimensionality of the image. Alternatively, a three-layer neural network can compress a 2D image into Gabor filter coefficients with 20:1 compression rates [111]. For visual texture analysis, different neural networks may be implemented, e.g. probabilistically weighted neural network [112], cellular neural network [113] and convolutional neural network [114]. Neurons sensitive to binocular disparity for stereoscopic depth perception are present in the V1 and V2 regions of the visual cortex [115]. Displacement of a function generates a proportional phase shift in its Fourier transform - a localised Fourier transform may be approximated by a Gabor function which represents a sinusoidal-shaped Gaussian envelope. For a pair of left/right binocular cells, their broad receptive fields can be represented by transforms:

$$f_{left}(x) = e^{-x^2/2\sigma^2}\cos(wx + \phi_{left}) \quad (9)$$
$$f_{right}(x) = e^{-x^2/2\sigma^2}\cos(wx + \phi_{right})$$

where σ, w and ϕ are size, angular frequency and phases of the receptive fields. The response of the neuron to a stimulus is given by:

$$r = \int_{-\infty}^{\infty} |f_{left}(x)I_{left}(x) + f_{right}(x)I_{right}(x)|dx \quad (10)$$

where I(x)=intensity of retinal image, $I_{right}(x)=I(x)$, $I_{left}(x)=I(x+d)$, d=binocular disparity. Assuming that the receptive field widths are much larger than the disparity:

$$r \approx 2Acos\left(\theta + \frac{\phi_{left}+\phi_{right}}{2} - \frac{wd}{2}\right)cos\left(\frac{\phi_{left}-\phi_{right}}{2} + \frac{wd}{2}\right) \quad (11)$$

where A and θ are amplitude and phase of the Fourier transform of image I(x) at frequency w. The Fourier transform is sensitive to the phase shift. Robustness requires independence of Fourier phase. By introducing a 90o phase shift between the two neurons and squaring and summing the output gives a disparity tuned with a broader width:

$$r \approx 4A^2cos^2\left(\frac{\phi_{left}-\phi_{right}}{2} + \frac{wd}{2}\right) \quad (12)$$

with $d = \frac{\phi_{left}-\phi_{right}}{w}$. The receptive fields may integrate motion with stereo sensitivity:

$$f_{left}(x,t) = e^{-\frac{x^2}{2\sigma_x^2}-\frac{t^2}{2\sigma_t^2}}\cos(w_x x + w_t t + \phi_{left}) \quad (13)$$
$$f_{right}(x,t) = e^{-\frac{x^2}{2\sigma_x^2}-\frac{t^2}{2\sigma_t^2}}\cos(w_x x + w_t t + \phi_{right})$$

The images representing binocular disparity and motion are given by: $I_{left}(x,t)=I(x-vt)$ and $I_{right}(x,t)=I(x-vt+d)$. The response becomes:

$$r \approx 2A\delta(w_t + w_x v_x)cos\left(\theta + \frac{\phi_{left}+\phi_{right}}{2} - \frac{wd}{2}\right)cos\left(\frac{\phi_{left}-\phi_{right}}{2} + \frac{w_x d}{2}\right)$$
$$r \approx 4A^2\delta^2(w_t + w_x v_x)cos^2\left(\frac{\phi_{left}-\phi_{right}}{2} + \frac{w_x d}{2}\right) \quad (14)$$

Hence, neural network responses may be tuned to both disparity and motion detection.

Analogue neural network hardware may be constructed from op-amps which in turn may be constructed from vacuum tubes (of which the PMT is an

example) which can be constructed from lunar resources. Although we have yet to 3D print vacuum tubes, we have implemented op-amp-based analogue neural network circuits, specifically Yamashita-Nakamura neurons [116] in fixed weight circuits [117] and with backpropagation learning circuitry [118] demonstrating the principle of adopting analogue neural networks as computational hardware potentially manufacturable from lunar resources.

IX. SPECTRAL ANALYSIS

A simple photometer may be constructed comprising a light emitting diode source, a light-dependent resistor detector and an amplifier/buffer circuit to drive a voltmeter [119]. The sample under study is placed between the source and detector to measure the light transmitted through it according to the Beer-Lambert law which defines absorbance thus:

$$A = -log_{10}\left(\frac{I}{I_0}\right) = \varepsilon cl \quad (15)$$

where c=concentration of compound, l=sample path length, ε=wavelength-dependent constant, I_0=incident light intensity, I=transmitted light intensity. A slit and prism may be sandwiched between the source and detector to select specific wavebands to analyse. Spectral lines in reflected light contain invaluable information about the sample under study. All matter emits electromagnetic energy characteristic of its material composition. They both absorb (absorption lines) and emit (emission lines) electromagnetic radiation. These lines are sharp in rarified gases but they become broadened into a continuous spectrum in denser configurations such as liquids or solids. A spectrometer comprises a narrow slit ~0.2 mm in width which projects optical energy onto the dispersive element. Diffraction gratings are traditionally used in spectrometers to split and diffract light into different components. Gratings comprise of surface ridges with a periodic structure with a characteristic space d wider than the wavelength of light λ. Light incident to the grating at angle θ_i is diffracted and will have a maximum at angle θ_m:

$$d(sin\theta_i + sin\theta_m) = m\lambda \quad (16)$$

where m=order. For light incident normally to the grating, this reduces to:

$$dsin\theta_m = m\lambda \quad (17)$$

A CD has a nominal track separation of 1.6 μm corresponding to a line density of 625/mm. An early diffraction grating was created by von Fraunhofer in 1821 constructed from wires. Ruling engines were subsequently developed to manufacture diffraction gratings in which a highly accurate diamond cutter was used to shave grooves into a glass plate. This is potentially feasible with on the Moon using 3D printed geared motors. A flexible diffraction grating may be formed from polydimethylsiloxane (PDMS) silicone elastomer with 2-20 μm lines and spacing – it can be used to measure pressure [120] and temperature [121]. Replica moulding requires a photolithographically patterned silicon die as the master. This is not feasible on the Moon. Hence, spectroscopic measurement will require prisms as the dispersive element rather than diffraction gratings. The prism disperses through refraction rather than diffraction as in a grating. A glass prism (of fused silica glass derived from lunar silicates) comprises several flat optical surfaces oriented with respect to each other that refract light. Typically, the prism is triangular with a triangular base and rectangular sides. It may be used to differentially disperse different frequencies of light. Light incident to the prism is refracted and leaves the prism at different angles according to the frequency of its different components, e.g. white light consists of light across the visible waveband – in which blue light is refracted more than red light. The refraction is dependent on the refractive indices of the two media. Deviation angle is given by:

$$\delta(\lambda) = \theta_i + \theta_r \approx (n(\lambda) - 1)\alpha \quad (18)$$

where n(λ)=refractive index, α=prism apex angle. Prisms disperse light over a wider frequency range than diffraction gratings and do not suffer from spectral order overlaps. For example, the Shuttle Imaging Spectrometer Experiment (SISEX) instrument used a prism rather than a grating for its dispersive optics [122]. Prisms may also be deployed as retroreflectors constructed from three mirrors forming the corners of a reflecting cube. 3D printing offers the capability of manufacturing 3D arrays of optical elements from fused silica glass. A Fourier series neural network (FSNN) may be employed as a neural network spectrum analyser to model complex systems with multiple variables [123]. The FSNN approximates the Fourier series of a time domain input/output to a dynamic system using neurons with complex harmonic activation functions of the form $y(x, w) = \sum_i \sum_j W_i \cos(w_i x) + W_j \sin(w_i x)$. The FSNN operates in parallel offering rapid computation. We suggest that simple forms of spectroscopy based on glass prisms may potentially be leveraged from lunar resources (Appendix).

X. CONCLUSIONS

It is plausible to manufacture from lunar resources sensors to measure the most fundamental parameters required for robotic machines. Electrical resistance of conducting wire of aluminium derived from lunar anorthite offers the measurement of displacement (potentiometer) and temperature (resistance thermistor/bolometer). Quartz manufactured via silica from lunar silicates offers the measurement of mass (quartz microbalance), time (quartz oscillation frequency), temperature (pyroelectricity). Photomultipliers offer the measurement of light

intensity (vision). There are biomimetic approaches to compensate for limitations in PMT light arrays such as active vision and optic flow navigation. Spectroscopic analysis using prisms rather than diffraction gratings also presents a possibility. One might – justly – regard sensor technology as the barometer of scientific sophistication for it has been through scientific instruments that we have interrogated the world. Sensor technology is also part of the triumvirate of robotics: sensors-controller-actuators. If the full spectrum of robotic capabilities, namely, sensor-controller-actuator, including vision capabilities can be manufactured from lunar resources, then robotic machines and machines of production can be constructed from lunar resources.

REFERENCES

[1] Khoshnevis B, Bodiford M, Burks K, Ethridge E (2005) "Lunar contour crafting: a novel technique for ISRU-based habitat development" *Proc 43rd AIAA Aerospace Sciences Meeting & Exhibit*, AIAA 2005-538

[2] Cesaretti G, Dini E, de Kestellier X, Colla V, Pambaguian L (2014) "Building components for an outpost on the lunar soil by means of a novel 3D printing technology" *Acta Astronautica* **93**, 430-450

[3] Ellery A (2020) "Sustainable in-situ resource utilisation on the Moon" *Planetary & Space Science* **184**, 104870

[4] Pak V, Kirov S, Nalivaiko A, Ozherelkov D, Gromov A (2019) "Obtaining alumina from kaolin clay via aluminium chloride" *Materials (Basel)* **12** (23), paper no 3938

[5] Barmpakos D, Kaltsas G (2021) "Review on humidity, temperature and strain printed sensors – current trends and future perspectives" *Sensors* **21**, 739

[6] Skordos A, Chan P, Vincent J, Jeronimidis G (2002) "Novel strain sensor based on the campaniform sensillum of insects" *Phil Trans Royal Society London* **360**, 239-253

[7] Clements T, Rahn C (2005) "Three-dimensional contact imaging with an actuated whisker" *Proc IEEE/RSJ Int Conf Intelligent Robots & Systems*, 10.1109/IROS.2005.1545213

[8] Wicaksono D, Chen Y, French P (2007) "Design and modeling of a bio-inspired MEMS gyroscope" *Proc Int Conf Electrical Engineering & Informatics*, Indonesia, paper no. A-05, 226-229

[9] Franceschini N (1996) "Engineering applications of small brains" *FED J* **7** (2), 38-52

[10] Araromi O, Graule M, Dorsey K, Castellanos S, Foster J, Hsu W-H, Passy A, Vlassak J, Weaver J, Walsh C, Wood R (2020) "Ultra-sensitive and resilient compliant strain gauges for soft machines" *Nature* **587**, 219-224

[11] Riedel R, Toma L, Janssen E, Nuffer J, Melz T, Hanselka H (2010) "Piezoresistive effect in SiOC ceramics for integrated pressure sensors," *J American Ceramics Society* **93** (4), 920-924

[12] Luheng W, Tainhuai D, Peng W (2009) "Influence of carbon black concentration on piezoresistivity for carbon-black filled silicone rubber composite" *Carbon* **47**, 3151-3157

[13] Muth J, Vogt D, Truby R, Menguc Y, Kolesky D, Wood R, Lewis J (2014) "Embedded 3D printing of strain sensors within highly stretchable elastomers" *Advanced Materials* **26**, 6307-6312

[14] Ramadan K, Sameoto D, Evoy S (2014) "Review of piezoelectric polymers as functional materials for electromechanical transducers" *Smart Materials & Structures* **23**, 033001

[15] Dahiya R, Cattin D, Adami A, Collini C, Barboni L, Valle M, Lorenzelli L, Oboe R, Metta G, Brunetti F (2011) "Towards tactile sensing system on chip for robotic applications" *IEEE Sensors J* **11** (12), 3216-3226

[16] Someya T, Sekitani T, Iba S, Kato S, Kawaguchi H, Sakurai T (2004) "Large area, flexible pressure sensor matrix with organic field effect transistors for artificial skin applications" *Proc National Academy Sciences* **101** (27), 9966-9970

[17] Guo X, Xu Y, Ogier S, Ng N, Caironi M, Perinot A, Li L, Zhao J, Tang W, Sporea R, Nejim A, Carrabina J, Cain P, Yan F (2017) "Current status and opportunities of organic thin-film transistor technologies" *IEEE Trans Electron Devices* **64** (5), 1906-1921

[18] Park Y-L, Chen B-R, Wood R (2012) "Design and fabrication of soft artificial skin using embedded microchannels and liquid conductors" *IEEE Sensors J* **12** (8), 2711-2718

[19] Gawade S, Jadhav A (2012) "Review on electrorheological fluids" *Int J Engineering Research & Technology* **1** (10), 2278-0181

[20] Zhou J, Gu Y, Fei P, Mai W, Gai Y, Yang R, Bao G, Wang Z (2008) "Flexible piezotronic strain sensor" *Nano Letters* **8** (9), 3035-3040

[21] Omata S, Murayama Y, Constantinou C (2004) "Real time robotic tactile sensor system for the determination of the physical properties of biomaterials" *Sensors & Actuators* **A112**, 278-285

[22] Kosorotov V, Blonsky I, Shchedrina L, Levash L (2003) "Quartz as artificial pyroactive material" *Proc SPIE* **5065**, 6th Int Conf Materials & Material Properties for Infrared Optoelectronics, 108-116

[23] Fishel J, Loeb G (2012) "Bayesian exploration for intelligent identification of textures" *Frontiers in Neurorobotics* **6** (4), 1-20

[24] Denei S, Mastrogiovanni F, Cannata G (2015) "Towards the creation of tactile maps for robots and their use in robot contact motion control" *Robotics & Autonomous Systems* **63**, 293-308

[25] Rayneau-Kirkhope D (2021) "Replicating how plants move" *Physics World* (Jul), 25-29

[26] Denis M, Ormston T, Scuka D, Jameux D, Witasse O (2009) "Ordinary camera, extraordinary places" *ESA Bulletin* **139** (Aug), 29-33

[27] Frederickson S, Abbott L, Duran S, Jochim D, Studak B, Wagenknecht J, Williams N (2003) "Mini AERCam: development of a freeflying nanosatellite inspection robot" *Proc SPIE* **5088** Space Systems Technology & Operations, Orlando, FL

[28] Ellery A (2022) "Is electronics fabrication feasible on the Moon?" in press with *Proc ASCE Earth & Space Conf*, Colorado School of Mines, Denver

[29] Ellery A (2021) "Generating and storing power on the Moon using in-situ resources" *Proc IMechE J Aerospace Engineering* DOI: 10.1177/0954410021 1029433

[30] Zhou Y, Zhao H, Ma D, Rosei F (2018) "Harnessing the properties of colloidal quantum dots in luminescent solar concentrators" *Chemical Society Review* **47**, 5866-5890

[31] Zhao H, Rosei F (2017) "Colloidal quantum dots for solar technologies" *Chemistry* **3**, 229-258

[32] Navarro-Pardo F, Zhao H, Wang Z, Rosei F (2018) "Structure/property relations in giant semiconductor nanocrystals: opportunities in photonics and electronics" *ACS Chemical Research* **51**, 609-618

[33] Lubsandorzhiev B (2006) "On the history of photomultiplier tube invention" *Nuclear Instruments & Methods in Physics Research A: Accelerators, Spectrometers, Detectors & Associated Equipment* **567**(1), 236

[34] Lee W, Attenkofer K, Walters D, Demarteau M, Yusof Z (2012) "Optimisation of transmission mode metallic (aluminium) photocathodes" *Physics Procedia* **37**, 757-764

[35] Donchev E, Pang J, Gammon P, Centeno A, Xie F, Petrov P, Breeze J, Ryan M, Riley J, Alford N (2013) "Rectenna device: from theory to practice (a review)" *MRS Energy & Sustainability: A Review J* **1**, E1

[36] Clavero C (2014) "Plasmon-induced hot electron generation at nanoparticle/metal oxide interfaces for photovoltaic and photocatalytic devices" *Nature Photonics* **8** (Feb), 95-103

[37] Knight M, Sobhani H, Nordlander P, Halas N (2011) "Photodetection with optical antennas" *Science* **332** (May), 702-704

[38] Livshits P, Dikhtyar V, Inberg A, Shahadi A, Jerby E (2011) "Local doping of silicon by a point-contact microwave applicator" *Microelectronic Engineering* **88**, 2831-2836

[39] Bhatnagar A, Reddy V, Srivasatava V (1985) "Optical energy gap of amorphous selenium: effect of annealing" *J Physics D: Applied Physics* **18**, L149-L153

[40] Woollam J, Morash K, Kuminsky M, Averbach B (1971) "Photoconductive and optical properties of amorphous selenium" *NASA TN D-6500*

[41] Schindewolf U (1960) "Selenium and tellurium content of stony meteorites by neutron bombardment" *Geochimica et Cosmochimica Acta* 19, 134-138

[42] Jotter R & Ott U (2011) "Selenium isotopes in some chondrites" *74th Annual Meteoritical Society Abstracts*, no. 5016

[43] Rickard D (1997) "Kinetics of pyrite formation by the H2S oxidation of iron (II) monosulphide in aqueous solutions between 25 and 125ºC: the rate equation" *Geochimica et Cosmochimica Acta* **61** (1), 115-134

[44] Wachterhauser G (1990) "Evolution of the first metabolic cycles" *Proc National Academy Sciences* **87**, 200-204

[45] Chatzitheodorou G, Fiechter S, Konenkamp R, Kunst M, Jaegermann W, Tributsch H (1986) "Thin photoactive FeS_2 (pyrite) films" *Material Research Bulletin* **21**, 1481-1487

[46] Ta X, Chan W, van der Graaf H (2016) "Secondary electron emission materials for transmission dynodes in novel photomultipliers: a review" *Materials* **9**, paper no 1017

[47] Hecht J (2010) "Short history of laser development" *Optical Engineering* **49** (9), 091002

[48] Klainer, S, Dandge D, Butler M, Goswami K (1991) "Fibre optic refractive index sensor using metal cladding" *US Patent 5026139A (expired)*

[49] Imel D (2005) "What is the procedure by which synthetic rubies are produced?" *The Rock Collector* (May), 6-9

[50] Barletta W, Bisognano J, Corlett J, Emma P, Huang Z, Kim K-J, Lindberg R, Murphy J, Neil G, Nguyen D, Pellegrini C, Rimmer R, Sannibale F, Stupakov G, Walker R, Zholents A (2010) "Free electron lasers: present status and future challenges" *Nuclear Instruments & Methods in Physics Research* **A618**, 69-96

[51] Nilsson D, Pelger S (1994) "Pessimistic estimate of the time required for an eye to evolve" *Proc Royal Society* B **256**, 53-58

[52] Fernald R (2000) "Evolution of eyes" *Current Opinion in Neurobiology* **10**, 444-450

[53] Rodriguez-Sanchez A, Simine E, Tsotsos J (2007) "Attention and visual search" *Int J Neural Systems* **17** (4), 1-14

[54] Albright T, Stoner G (1995) "Visual motion perception" *Proc National Academy Sciences* **92**, 2433-2440

[55] Nowlan S, Sejnowski T (1995) "Selection model for motion processing in area MT of primates" *J Neuroscience* **15** (2), 1195-1214

[56] Van Steveninck R, Borst A, Bialek W (2000) "Real time encoding of motion: answerable questions

and questionable answers from the fly's visual system" *arXiv:physics/0004060v1 [physics.bio-ph] 25 Apr 2000*

[57] Van Essen D, Gallant J (1994) "Neural mechanisms of form and motion processing in the primate visual system" *Neuron* **13** (Jul), 1-10

[58] Van Essen D (2005) "Corticocortical and thalamocortical information flow in the primate visual cortex" *Progress in Brain Research* **149**, 173-179

[59] Kruger N, Janssen P, Kalkan S, Lappe M, Leonardis A, Piater J, Rodriguez-Sanchez A, Wiskott L (2013) "Deep hierarchies in the primate visual cortex: what can we learn for computer vision?" *IEEE Trans Pattern Analysis & Machine Intelligence* **35** (8), 1847-1871

[60] Tovee M (1994) "How fast is the speed of thought?" *Current Biology* **4** (12), 1125-1127

[61] Clark A (1999) "Visual awareness and visuomotor action" *J Consciousness Studies* **6** (11-12), 1-18

[62] O'Regan K, Noe A (2001) "Sensorimotor account of vision and visual consciousness" *Behavioural & Brain Sciences* **24**, 939-1031

[63] Ungerleider L, Haxby J (1994) "What and where in the human brain" *Current Opinion in Neurobiology* **4**, 157-165

[64] Itti L, Koch C (2000) "Saliency-based search mechanism for overt and covert shifts of visual attention" *Vision Research* **40**, 1489-1506

[65] Itti L, Koch C (2001) "Computational modelling of visual attention" *Nature Reviews Neuroscience* **2** (Feb), 1-11

[66] Liu N, Han J, Liu T, Li X (2018) "Learning to predict eye fixations via multiresolution convolutional neural networks" *IEEE Trans Neural Networks & Learning Systems* **29** (2), 392-404

[67] Bruce N, Tsotsos J (2009) "Saliency, attention and visual search: an information theoretic approach" *J Vision* **9** (3), 1-24

[68] Olshausen B, Anderson C, van Essen D (1993) "Neurobiological model of visual attention and invariant pattern recognition based on dynamic routing of information" *J Neuroscience* **13** (11), 4700-4719

[69] Ji W, Weng J (2015) "Developmental where-what network for concurrent and interactive visual attention and recognition" *Robotics & Autonomous Systems* **71**, 35-48

[70] Chao F, Lee M, Lee J (2010) "Developmental algorithm for ocular-motor coordination" *Robotics & Autonomous Systems* **58**, 239-248

[71] Jodogne S, Piater J (2007) "Closed loop learning of visual control policies" *J Artificial Intelligence Research* **28**, 349-391

[72] Rauschecker J, Tian B (2000) "Mechanisms and streams for processing of "what" and "where" in auditory cortex" *Proc National Academy Sciences* **97** (22), 11800-11806

[73] Kraus N, Nicol T (2005) "Brainstem origins for cortical "what" and "where" pathways in the auditory cortex" *Trends in Neurosciences* **28** (4), 177-181

[74] Sandini G, Tagliasco V (1980) "Anthropomorphic retina-like structure for scene analysis" *Computer Graphics & Image Processing* **14**, 365-372

[75] Ballard D (1991) "Animate vision" *Artificial Intelligence* **48** (1), 57-86

[76] Carpenter R, Williams M (1995) "Neural computation of log likelihood in control of saccadic eye movements" *Nature* **377**, 59-61

[77] Whaite P, Ferrie F (1997) "Autonomous exploration: driven by uncertainty" *IEEE Trans Pattern Analysis & Machine Intelligence* **19** (3), 193-205

[78] Seung H (1996) "How the brain keeps the eyes open" *Proc National Academy Sciences* **93**, 13339-13344

[79] Arai K, Keller E, Edelman J (1994) "Two-dimensional neural network model of the primate saccadic system" *Neural Networks* **7** (6/7), 1115-1135

[80] Lefevre P, Galiana H (1992) "Dynamic feedback to the superior colliculus in a neural network model of the gaze control system" *Neural Networks* **5**, 871-890

[81] Schall J (2004) "On building a bridge between brain and behaviour" *Annual Reviews Psychology* **55**, 23-50

[82] Young M, Depalma A, Garrett S (2002) "Situations, interaction, process and affordances: an ecological psychology perspective" *Instructional Science* **30**, 47-63

[83] Janabi-Sharifi F, Marey M (2010) "Kalman filter-based method for pose estimation in visual servoing" *IEEE Trans Robotics* **26** (5), 939-946

[84] Anjum M, Ahmad O, Bona B, Cho D (2013) "Sensor data fusion using unscented Kalman filter for VOR-based vision tracking system for mobile robots" *Proc Towards Autonomous Robotic Systems 14th Conf*, Oxford, UK

[85] Lisberger S, Sejnowski T (1992) "Motor learning in a recurrent network model based on the vestibulo-ocular reflex" *Nature* **360** (Nov), 159-161

[86] Ross J & Ellery A (2017) "Panoramic camera tracking on planetary rovers using feedforward control" *Int J Advanced Robotic Systems* (May/Jun), 1-9

[87] Shibata T, Vijayakumar S, Conradt J, Schaal S (2001) "Biomimetic oculomotor control" *Adaptive Behaviour* **9** (3/4), 189-207

[88] Elaskri A, Ellery A (2020) "3D printed electric motors as a step towards self-replicating machines" *Proc Int Symp Artificial Intelligence, Robotics and Automation in Space*, paper no 5020

[89] Duchon A, Warren W, Kaelbling L (1998) "Ecological robotics" *Adaptive Behaviour* **6** (3/4), 473-507

[90] Menzel R & Giufa M (2001) "Cognitive architecture of a mini-brain: the honeybee" *Trends in Cognitive Sciences* **5** (2), 62-71

[91] Wessnitzer J, Webb B (2006) "Multimodal sensory integration in insects – towards insect brain control architectures" *Bioninspiration & Biomimetics* **1**, 63-75

[92] Neumann T (2002) "Modelling insect compound eyes: space variant spherical vision" *Proc 2nd Int Workshop on Biologically Motivated Computer Vision* (ed. Bulthoff H, Lee S-W, Poggio T, Wallraven C), LNCS 2525, 360-367

[93] Srinivasan M (1992) "How bees exploit optic flow: behavioural experiments and neural network models" *Philosophical Transactions Royal Society* **B337**, 253-258

[94] Prabhakara R, Wright C, Barrett S (2012) "Motion detection: a biomimetic vision sensor versus a CCD camera sensor" *IEEE Sensors J* **12** (2), 298-307

[95] Lappe M, Bremmer F & van den Berg A (1999) "Perception of self-motion from visual flow" *Trends in Cognitive Science* **3** (9), 329-336

[96] Cornilleau-Peres V & Giden C (1996) "Interaction between self-motion and depth perception in the processing of optic flow" *Trends in Neuroscience* **19** (5), 196-402

[97] Franceschini N (2009) "Towards automatic visual guidance of aerospace vehicles: from insects to robots" *Acta Futura* **3**, 15-34

[98] Franceschini N, Pichon J & Blanes C (1992) "From insect vision to robot vision" *Philosophical Transactions Royal Society* **B337**, 283-294

[99] Huber S, Franz M, Buthoff H (1999) "On robots and flies: modelling the visual orientation behaviour of flies" *Robotics & Autonomous Systems* **29**, 227-242

[100] Parberry I (1994) *Circuit complexity and neural networks*, MIT Press Foundations of Computing, Cambridge, MA

[101] Siegelmann H & Sontag E (1995) "On the computational power of neural nets" *J Computer & System Sciences* **50**, 132-150

[102] Watanabe T, Tanaka M, Kurita T, Mishima T (2002) "Autonomous foveating system based on pulse-coupled neural network with sigmoidal pulse generator" *Trans Society Instrument & Control Engineers* **38** (8), 762-732

[103] Schoner G, Dose M, Engels C (1995) "Dynamics of behaviour: theory and applications for autonomous robot architectures" *Robotics & Autonomous Systems* **16**, 213-245

[104] Quoy M, Moga S, Gaussier P (2003) "Dynamical neural networks for planning and low-level robot control" *IEEE Trans Systems Man & Cybernetics A: Systems & Humans* **33** (4), 523-532

[105] Erlhagen W & Bicho E (2006) "Dynamic neural field approach to cognitive robotics" *J Neural Engineering* **3**, R36-R54

[106] Pomerleau D (1989) "ALVINN: an autonomous land vehicle in a neural network" *Proc Neural Information Processing* Systems, 305-313

[107] Husbands P, Harvey I, Cliff D (1995) "Circle in the round: state space attractors for evolved sighted robots" *Robotics & Autonomous Systems* **15**, 83-106

[108] Cameron S, Grossberg S, Guenther F (1998) "Self-organizing neural network architecture for navigation using optic flow" *Neural Computation* **10**, 313-352

[109] Tettenborn A & Ellery A (2018) "Comparison of Gabor filters and wavelet transform methods for extraction of lithological features" *Proc Int Symp Artificial Intelligence Robotics & Automation in Space*, paper no. P9

[110] Kameyama K, Mori K, Kosugi Y (1997) "Neural network incorporating adaptive Gabor filters for image texture classification" *Proc Int Conf Neural Networks*, 614119

[111] Daugman J (1988) "Complete discrete 2D Gabor transformation by neural networks for image analysis and compression" *IEEE Trans Acoustics, Speech & Signal Processing* **36** (7), 1169-1179

[112] Kiranmayee M, Subbarao M (2012) "Texture classification using weighted probabilistic neural networks" *Int J Image Processing & Vision Sciences* **1** (2), 38-40

[113] Materka A, Strzelecki M (1998) "Texture analysis methods – a review" *COST B11 report*, Institute of Electronics, Technical University of Lodz, Brussels

[114] Tivive C, Bouzerdoum A (2006) "Texture classification using convolutional neural networks" *IEEE Region 10 Conf*, Hong Kong, China

[115] Qian N (1994) "Computing stereo disparity and motion with known binocular cell properties" *Neural Computation* **6**, 390-404

[116] Yamashita Y, Nakamura Y (2007) "Neuron circuit model with smooth nonlinear output function" *Proc Int Symp Nonlinear Theory & its Applications*, Vancouver, pp. 11-14

[117] Larson S & Ellery A (2015) "Trainable analogue neural network with application to lunar in-situ resource utilisation" *Proc Int Astronautics Federation Congress*, Jerusalem, IAC-15-D3.3.6

[118] Prasad V, Ellery A (2020) "Analogue neural network architecture for in-situ resourced computing hardware on the Moon" *Proc Int Symp Artificial Intelligence, Robotics and Automation in Space*, paper no 5005

[119] Tavener S & Thomas-Oates J (2007) "Build your own photometer" *Education in Chemistry* (Sep), 151-154

[120] Hosokawa K, Hanada K, Maeda R (2002) "Polydimethylsiloxane (PDMS) deformable diffraction grating for monitoring of local pressure in microfluidic devices" *J Micromechanics & Microengineering* **12**, 1-6

[121] Rogers J, Jackman R, Schueller O, Whitesides G (1996) "Elastomeric diffraction gratings as photothermal detectors" *Applied Optics* **35** (34), 6641-6647

[122] Herring M (1987) "Shuttle imaging spectrometer experiment (SISEX)" *Proc SPIE 0834 – Imaging Spectroscopy II*, San Diego, CA

[123] Bouchard J, Zhu C, Paul F (1995) "Neural network spectrum analyser" *Mechatronics* **5** (6), 603-622

[124] Ellery A, Mellor I, Wanjara P, Conti M (2022) "Metalysis FFC process as a strategic lunar in-situ resource utilisation technology" *New Space J* **10** (2), 224-238

[125] Salinas E, Sejnowski T (2001) "Gain modulation in the central nervous system: where behaviour, neurophysiology and computation meet" *Neuroscientist* **7** (5), 430-440

APPENDIX: LUNAR INDUSTRIAL ECOLOGY

(emboldened oxides are feedstock for the Fray Farthing Chen (FFC) process [124])

Ilmenite

$Fe^0 + H_2O$ → ferrofluidic sealing

$FeTiO_3 + H_2 \rightarrow$ **TiO_2** $+ H_2O + Fe$ and $2H_2O \rightarrow 2H_2 + O_2$

↑_____|

$2Fe + 1.5O_2 \rightarrow Fe_2O_3/Fe_2O_3.CoO$ → ferrite magnets

$3Fe_2O_3 + H_2 \leftrightarrow Fe_3O_4 + H_2O$) → magnetite at 350-750°C/1-2 kbar

M-type Meteorites $4Fe_2O_3 + Fe \leftrightarrow 3Fe_3O_4$)

W inclusions → thermionic cathodic material

Carbonyl process:

Iron alloy	Ni	Co	Si	C	W
→ Tool steel				2%	9-18%
→ Electrical steel			3%		
→ Permalloy	80%				
→ Kovar	29%	17%	0.2%	0.01%.	

$Fe(CO)_5 \leftrightarrow 5CO + Fe$ (175°C/100 bar)

$Ni(CO)_4 \leftrightarrow 4CO + Ni$ (55°C/1 bar)

$Co_2(CO)_8 \leftrightarrow 8CO + 2Co$ (150°C/35 bar)

S catalyst

$4FeS + 7O_2 \rightarrow$ **$2Fe_2O_3$** $+ 4SO_2$

Troilite $SO_2 + H_2S \rightarrow 3S + H_2O$

$FeSe + Na_2CO_3 + 1.5O_2 \rightarrow$ **FeO** $+ Na_2SeO_3 + CO_2$

KNO_3 catalyst $Na_2SeO_3 + H_2SO_4 \rightarrow Na_2O + H_2SO_4 + Se$ → photosensitive Se

↑_____|

$Na_2O + H_2O \rightarrow 2NaOH$

Lunar Orthoclase NaOH + HCl → NaCl + H_2O (recycle)

$3KAlSi_3O_8 + 2HCl + 12H_2O \rightarrow KAl_3Si_3O_{10}(OH)_2 + 6H_4SiO_4 + 2KCl$

orthoclase illite silicic acid (soluble silica → **SiO_2** $+ H_2O$)

$2KAl_3Si_3O_{10}(OH)_2 + 2HCl + 3H_2O \rightarrow 3Al_2Si_2O_5(OH)_4 + 2KCl$ → kaolinite binder → porcelain

kaolinite $KCl + NaNO_3 \rightarrow NaCl + KNO_3$ (recycled)

Lunar Anorthite

$CaAl_2SiO_8 + 4C \rightarrow CO +$ **CaO** $+$ **Al_2O_3** $+ 2Si$ at 1650°C → CaO cathode coatings

$CaO + H_2O \rightarrow Ca(OH)_2$

$Ca(OH)_2 + CO_2 \rightarrow CaCO_3 + H_2O$

$CaAl_2SiO_8 + 5HCl + H_2O \rightarrow CaCl_2 + 2AlCl_3.6H_2O +$ **SiO_2** → fused silica glass + FFC electrolyte

$AlCl_3.6H_2O \rightarrow Al(OH)_3 + 3HCl + H_2O$ at 100°C

↑_____|

$Al(OH)_3 \rightarrow$ **Al_2O_3** $+ 3H_2O$ at 400°C → $2Al + Fe_2O_3$ → $2Fe + Al_2O_3$ (thermite)

Lunar Olivine → AlNiCo hard magnets

$3Fe_2SiO_4 + 2H_2O \rightarrow 2Fe_3O_4 + 3$**$SiO_2$** $+ 2H_2O$

fayalite magnetite

$Mg_2SiO_4 + 4H_2O \rightarrow$ **$2MgO$** $+$ **SiO_2** $+ 4H_2O$ → 3D Shaping binder (Sorel cement)

forsterite $MgO + HCl \rightarrow MgCl_2 + H_2O$ → 3D Shaping binder (Sorel cement)

Lunar Pyroxene

$Ca(Fe,Al)Si_2O_6 + HCl + H_2O \rightarrow Ca_{0.33}(Al)_2(Si_4O_{10})(OH)_2.nH_2O + H_4SiO_4 + CaCl_2 + Fe(OH)_3$

augite montmorillonite silicic acid iron hydroxide

$6MgSiO_3 + H_2O \rightarrow Mg_3Si_2O_5(OH)_4 + Mg_3Si_4O_{10}(OH)_2$ → dry lubricant talc

enstatite serpentine talc

Lunar Volatiles

$CO + 0.5\ O_2 \rightarrow CO_2$

$CO_2 + 4H_2 \rightarrow CH_4 + 2H_2O$ at 300°C (Sabatier reaction) → $CH_4 \rightarrow C + 2H_2$ at 1400°C → steel additive/anode regeneration

Ni catalyst

850°C 250°C

$CH_4 + H_2 \rightarrow CO + 3H_2 \rightarrow CH_3OH$ 350°C

Ni catalyst Al_2O_3 catalyst $CH_3OH + HCl \rightarrow CH_3Cl + H_2O$ 370°C $+nH_2O$ (Rochow process)

Al_2O_3 catalyst $CH_3Cl + Si \rightarrow (CH_3)_2SiCl_2 \rightarrow ((CH_3)_2SiO)_n + 2nHCl$ → silicone plastics/oils

$N_2 + 3H_2 \rightarrow 2NH_3$ (Haber-Bosch process) ↑_____|
Fe on $CaO+SiO_2+Al_2O_3$ catalyst
$4NH_3 + 5O_2 \rightarrow 4NO + 6H_2O$
WC on Ni catalyst
$3NO + H_2O \rightarrow 2HNO_3 + NO$ (Ostwald process)
↑_____|
$2SO_2 + O_2 \leftrightarrow 2SO_3$ (low temp)
$SO_3 + H_2O \rightarrow H_2SO_4$

Earth-Supplied Salt Reagents

$2NaCl + CaCO_3 \leftrightarrow Na_2CO_3 + CaCl_2$ (Solvay process) → FFC electrolyte
350°C/150 MPa
$Na_2CO_3 + SiO_2(i) \leftrightarrow Na_2SiO_3 + CO_2$ → piezoelectric quartz
1000-1100°C (40-80 day growth)
$CaCO_3 \rightarrow$ **CaO** $+ CO_2$ (calcination)
$NaCl(s) + HNO_3(g) \rightarrow HCl(g) + NaNO_3(s)$ → recycled acid leach